

# Accelerated boundary integral analysis of energy eigenvalues for confined electron states in quantum semiconductor heterostructures

J. D. Phan<sup>†</sup>, A.-V. Phan<sup>‡1</sup>

<sup>†</sup> Daniel Guggenheim School of Aerospace Engineering  
Georgia Institute of Technology  
Atlanta, GA 30332, USA

<sup>‡</sup> Department of Mechanical, Aerospace and Biomedical Engineering  
University of South Alabama  
Mobile, AL 36688, USA

## Abstract

This paper presents a novel and efficient approach for the computation of energy eigenvalues in quantum semiconductor heterostructures. Accurate determination of the electronic states in these heterostructures is crucial for understanding their optical and electronic properties, making it a key challenge in semiconductor physics. The proposed method is based on utilizing series expansions of zero-order Bessel functions to numerically solve the Schrödinger equation using boundary integral method for bound electron states in a computationally efficient manner. To validate the proposed technique, we applied it to address previously explored issues by other research groups. The results clearly demonstrate the computational efficiency and high precision of our approach. Notably, the proposed technique significantly reduces the computational time compared to the conventional method for searching the energy eigenvalues in quantum structures.

**Keywords:** Quantum wire; Energy eigenvalue; Boundary integral method; Wavefunction; Probability density.

## 1. Introduction

In quantum mechanics, the behavior of particles within confined structures often leads to interesting and complex physical phenomena. The study of energy eigenvalues in such systems is not only an interesting exercise in mathematical physics but also holds significant implications for the design and understanding of nanoscale devices and quantum structures. This investigation utilized boundary element analysis to explore the energy eigenvalues associated with the quantum states of various quantum structures, shedding light on the fundamental principles that govern the quantum behavior of particles in complex confined systems.

Although the proposed technique can be applied to quantum heterostructures, the primary focus of this research lies in the domain of quantum wires. Quantum wire systems have attracted considerable attention in the scientific community due to their promising applications in nanoelectronics and quantum computing, *e.g.*, [1, 2]. Understanding the behavior and optimizing the performance of quantum wires relies on the accurate determination of their energy eigenvalues.

In this pursuit, researchers commonly employ finite and boundary element methods as preferred numerical techniques. For instance, previous studies, such as [3–7], have successfully applied the

---

<sup>1</sup>Corresponding author.

E-mail: jphan42@gatech.edu (J. D. Phan), vphan@southalabama.edu (A.-V. Phan)

finite element method for modeling quantum systems.

Boundary element methods (BEMs), on the other hand, offer distinct advantages when addressing open-boundary quantum wire systems. BEM is specifically tailored to solving the Schrödinger equation on the boundary of the wire, effectively simplifying the computational domain. Previous research endeavors, as demonstrated in references such as [4,8–13], have highlighted the use of BEM in this context.

It is essential to note that directly formulating the eigenvalue problem for the determination of energy eigenvalues proves to be a complex task. Consequently, the approach of scanning the energy variable  $E$  within a specified interval, in order to locate local minima of the eigenvalue determinant, as obtained through boundary element analysis (BEA), has emerged as a practical solution. While this search method exhibits a straightforward approach, it is not without its limitations. Notably, because the determinant is a function of the energy variable  $E$ , employing this method necessitates the complete repetition of the BEA for each value of  $E$ . This approach, though conceptually simple, imposes a substantial computational burden.

When the electron's effective masses remain constant in both the quantum wire and barrier regions, the Schrödinger equation simplifies to the Helmholtz equation. Although the generalized eigenvalue problem was formulated in [12], the technique presented in the paper is limited to generating real-valued wavefunctions. This limitation stems from its reliance on the real-valued Laplace operator rather than the complex-valued Helmholtz operator. In the broader context of quantum systems, it is important to note that wavefunctions can take on complex values, enabling them to encompass the phase information of the quantum state.

The proposed approach is founded on utilizing series expansions of zero-order Bessel functions in the fundamental solution to the Helmholtz equation. This novel method yields a set of independent fundamental functions that do not rely on the wave number of the Helmholtz equation. The resulting coefficient matrix in the system of boundary element equations takes the form of a matrix polynomial in terms of the parameter  $E$ . This characteristic enables a significantly expedited search for eigenvalues across a specified range of  $E$  values.

In this work, series expansions of zero-order Bessel functions were employed in the fundamental solution for the Helmholtz equation. This approach led to the development of novel multi-domain boundary integral equations (BIEs) comprising a series of boundary integrals that exhibit independence from the energy parameter  $E$ . By implementing these BIEs numerically through boundary elements, a system of equations known as the BEA system was formulated. Notably, the coefficient matrix of this system takes the form of a matrix polynomial in the variable  $E$ .

This innovative technique significantly streamlines the search for eigenvalues by scanning the parameter  $E$ . In contrast to the conventional method, where the boundary integrals necessitate re-evaluation for each value of  $E$  within the specified range, this approach reduces the computational time required. Several numerical examples were presented to demonstrate the effectiveness and accuracy of the proposed technique.

## 2. Boundary intergal formulation for energy eigenvalue analysis

### 2.1. Boundary integral equations

For a bound state of a quantum structure, with an interior region denoted as  $\mathcal{I}$  embedded within a barrier material in the exterior region denoted as  $\mathcal{E}$ , the wavefunctions of the electron are described

by the following Schrödinger equations, *e.g.*, [14]:

$$\nabla \cdot \left( \frac{1}{m_{\mathcal{I}}^*} \nabla \psi^{\mathcal{I}}(Q) \right) + \frac{2E}{\hbar^2} \psi^{\mathcal{I}}(Q) = 0 \quad (1)$$

$$\nabla \cdot \left( \frac{1}{m_{\mathcal{E}}^*} \nabla \psi^{\mathcal{E}}(Q) \right) + \frac{2(E - V_0)}{\hbar^2} \psi^{\mathcal{E}}(Q) = 0 \quad (2)$$

where  $m_{\mathcal{I}}^*$  and  $m_{\mathcal{E}}^*$  are the electron's effective masses in the interior and exterior regions, respectively,  $\hbar$  is the reduced Planck's constant,  $E$  is the energy of the electron and  $V_0$  is the barrier potential.

For constant values of  $m_{\mathcal{I}}^*$  and  $m_{\mathcal{E}}^*$ , the above equations reduce to Helmholtz's equations and can be solved via the following boundary integral equations using their respective fundamental solutions:

$$c(P)\psi^{\mathcal{I}}(P) = \int_{\Gamma} \left[ G_{\mathcal{I}}(P, Q) \psi_{,n}^{\mathcal{I}}(Q) - G_{\mathcal{I},n}(P, Q) \psi^{\mathcal{I}}(Q) \right] dQ \quad (3)$$

$$c(P)\psi^{\mathcal{E}}(P) = \int_{\Gamma} \left[ G_{\mathcal{E}}(P, Q) \psi_{,n}^{\mathcal{E}}(Q) - G_{\mathcal{E},n}(P, Q) \psi^{\mathcal{E}}(Q) \right] dQ \quad (4)$$

where the exterior region is treated as an infinite domain,  $P$  and  $Q$  represent the source and field points, respectively,  $c(P)$  stands for the solid angle coefficient [14],  $\Gamma$  denotes the interface that separates the interior and exterior regions, the subscript  $(\cdot)_{,n}$  signifies the derivative taken with respect to the unit outward normal  $\mathbf{n} = \mathbf{n}(Q)$  to  $\Gamma$ , *e.g.*,  $\psi_{,n} = \frac{\partial \psi}{\partial \mathbf{n}}$ , and  $dQ$  refers to an infinitesimal boundary length.

In situations involving two-dimensional (2-D) problems, such as the case of a straight quantum wire with a uniform cross-section, the fundamental solutions are given by

$$G_{\mathcal{I}}(P, Q) = \frac{i}{4} H_0^{(1)}(k_{\mathcal{I}} r) = -\frac{1}{4} \left( Y_0(k_{\mathcal{I}} r) - iJ_0(k_{\mathcal{I}} r) \right) \quad (5)$$

$$G_{\mathcal{E}}(P, Q) = \frac{1}{2\pi} K_0(k_{\mathcal{E}} r) = -\frac{1}{4} \left( Y_0(ik_{\mathcal{E}} r) - iJ_0(ik_{\mathcal{E}} r) \right) \quad (6)$$

In these equations,  $H_0^{(1)}$  is the zero-order Hankel function of the first kind,  $K_0$  denotes the zero-order modified Bessel function of the second kind,  $J_0$  and  $Y_0$  are the zero-order Bessel functions of the first and second kinds, respectively. Additionally,  $i$  represents the imaginary unit, and  $r$  refers to the distance between  $P$  and  $Q$ . The wavenumbers in the interior and exterior regions are defined respectively as follows:

$$k_{\mathcal{I}}^2 = 2m_{\mathcal{I}}^* E / \hbar^2 \quad (7)$$

$$k_{\mathcal{E}}^2 = 2m_{\mathcal{E}}^* (V_0 - E) / \hbar^2 \quad (8)$$

and the interface boundary conditions are

$$\psi^{\mathcal{E}} = \psi^{\mathcal{I}} \quad (9)$$

$$\psi_{,n}^{\mathcal{E}} = -\frac{m_{\mathcal{E}}^*}{m_{\mathcal{I}}^*} \psi_{,n}^{\mathcal{I}} = \mu \psi_{,n}^{\mathcal{I}} \quad (10)$$

It should be noted that the boundary integrals in Eqs. (3) and (4) require evaluation in the counterclockwise and clockwise directions, respectively.

## 2.2. Numerical implementation

If the interface boundary  $\Gamma$  is discretized into  $N$  boundary elements with a total of  $N_n$  boundary nodes, collocating Eqs. (3) and (4) at each source point  $P = 1 \dots N_n$  respectively yields the following equations:

$$\sum_{k=1}^{N_n} G_{Pk}^{\mathcal{I}} \psi_{,nk}^{\mathcal{I}} - \sum_{k=1}^{N_n} H_{Pk}^{\mathcal{I}} \psi_k^{\mathcal{I}} = 0 \quad (11)$$

$$\sum_{k=1}^{N_n} G_{Pk}^{\mathcal{E}} \psi_{,nk}^{\mathcal{E}} - \sum_{k=1}^{N_n} H_{Pk}^{\mathcal{E}} \psi_k^{\mathcal{E}} = 0 \quad (12)$$

By using the boundary conditions (9) and (10), Eq. (12) can be rewritten as

$$\mu \sum_{k=1}^{N_n} G_{Pk}^{\mathcal{E}} \psi_{,nk}^{\mathcal{I}} - \sum_{k=1}^{N_n} H_{Pk}^{\mathcal{E}} \psi_k^{\mathcal{I}} = 0 \quad (13)$$

The collocation at all  $N_n$  source points results in  $N_n$  equations of the form (11) and another  $N_n$  equations of the form (13). They are two systems of linear equations which can be written in matrix form as follows:

$$\mathbf{A}(E) \mathbf{u}_{\mathcal{I}} = \mathbf{0} \quad (14)$$

$$\mathbf{B}(E) \mathbf{u}_{\mathcal{I}} = \mathbf{0} \quad (15)$$

or

$$\mathbf{C}(E) \mathbf{u}_{\mathcal{I}} = \mathbf{0} \quad (16)$$

where  $\mathbf{A}$  and  $\mathbf{B}$  are the coefficient matrices of order  $(N_n \times 2N_n)$ ,

$$\mathbf{C}(E) = \begin{bmatrix} \mathbf{A}(E) \\ \mathbf{B}(E) \end{bmatrix} \quad (17)$$

and  $\mathbf{u}_{\mathcal{I}}$  represents the vector encompassing  $2N_n$  unknown nodal degrees of freedom  $\psi^{\mathcal{I}}$  and  $\psi_{,n}^{\mathcal{I}}$  on the interface  $\Gamma$ .

Non-trivial solutions for  $\mathbf{u}_{\mathcal{I}}$  in Eq. (16) can be determined from the following condition:

$$\det[\mathbf{C}(E)] = 0 \quad (18)$$

The roots  $E$  of the above equation represent the energy eigenvalues of the quantum system. By using these roots in Eq. (16), non-trivial  $\mathbf{u}_{\mathcal{I}}$  (eigenvectors) can be found (see, *e.g.*, [14]). A specific sub-vector of  $\mathbf{u}_{\mathcal{I}}$  containing exclusively the nodal wavefunctions  $\psi$  can be utilized to compute  $|\psi(Q)|^2$ , which conveys the probability density associated with locating an electron at a precise spatial coordinate denoted as  $Q$ . It is important to note that the probability density should be appropriately normalized to ensure that the total probability of finding the electron in the specified region is 100%. In other words,

$$\int_V |\psi(Q)|^2 dQ = 1 \quad (19)$$

where  $V$  includes both the structure and the region of interest within the barrier.

### 2.3. Conventional energy eigenvalue search

When  $\mathbf{C}(E)$  undergoes numerical evaluation, its determinant does not precisely equal zero for the roots  $E$  (see Eqs. (17) and (18)). Consequently, the common approach for identifying the real roots of Eq. (17) involves searching for the local minima of  $|\det[\mathbf{C}(E)]|$  within intervals where  $E_{\min} \leq E \leq E_{\max}$ , employing a small step size of  $\Delta E$ . In this scenario, the number of search iterations can be expressed as  $N_E = (E_{\max} - E_{\min})/\Delta E + 1$ . Since  $\mathbf{C}(E)$  is dependent on  $E$ , it is customary to opt for a very small value of  $\Delta E$ , resulting in a notably high value of  $N_E$ , in order to obtain highly accurate results and prevent any eigenvalues from being overlooked during the scanning process. As a result, this computational technique (conventional method) is widely recognized for its significant computational cost, as it necessitates the re-evaluation of the boundary integrals specified in Eqs. (3) and (4), along with the determinant in Eq. (17), at each iteration, amounting to a total of  $N_E$  iterations.

### 2.4. Accelerated energy eigenvalue search

In this research, a novel approach to expedite the search for energy eigenvalues was introduced, inspired by techniques previously developed in [17] and [18].

For the interior region, as the arguments  $k_{\mathcal{I}r}$  of  $Y_0$  and  $J_0$  are real numbers (see Eq. (5)), the technique presented in [17] and [18] can be applied to rewrite the BIE (3) as follows:

$$c(P)\psi^{\mathcal{I}}(P) = \sum_{j=0}^{\infty} \lambda_{\mathcal{I}}^j \int_{\Gamma} \left[ \bar{G}_{\mathcal{I}j}(P, Q) \psi_{,n}^{\mathcal{I}}(Q) - \bar{G}_{\mathcal{I}j,n}(P, Q) \psi^{\mathcal{I}}(Q) \right] dQ \quad (20)$$

where  $\lambda_{\mathcal{I}} = k_{\mathcal{I}}^2$ , and  $\bar{G}_{\mathcal{I}j}$  and  $\bar{G}_{\mathcal{I}j,n}$  are defined in Eqs. (32) and (34), respectively.

The advantage of Eq. (20) over Eq. (3) lies in the fact that the boundary integrals in Eq. (20) remain independent of the energy eigenvalues  $E$  that are being sought.

Nonetheless, the aforementioned technique cannot be applied to the BIE (4). This is due to the fact that, for the exterior region, the arguments  $ik_{\mathcal{E}r}$  of  $Y_0$  and  $J_0$  are pure imaginary numbers (as indicated in Eq. (6)), invariably resulting in  $J_0 > 0$ . Consequently, this condition contradicts the prerequisite of  $J_0 = 0$  as mandated for the applicability of the technique introduced in [17] and [18] in the context of the exterior region.

In the following, a novel technique is introduced to render BIE (4) independent of  $E$ . By incorporating Eq. (6) into Eq. (4), one gets

$$c(P)\psi^{\mathcal{E}}(P) = -\frac{1}{4} \int_{\Gamma} \left[ (Y_0(ik_{\mathcal{E}r}) - iJ_0(ik_{\mathcal{E}r})) \psi_{,n}^{\mathcal{E}}(Q) - (Y_{0,n}(ik_{\mathcal{E}r}) - iJ_{0,n}(ik_{\mathcal{E}r})) \psi^{\mathcal{E}}(Q) \right] dQ \quad (21)$$

Consider the series expansions of  $Y_0$  and  $J_0$  given by

$$Y_0(ik_{\mathcal{E}r}) = \frac{2}{\pi} \left[ \sum_{j=0}^{\infty} \frac{\lambda_{\mathcal{E}}^j r^{2j}}{(-4)^j (j!)^2} \left( \ln r - S_j + \gamma + \ln \frac{ik_{\mathcal{E}}}{2} \right) \right] \quad (22)$$

and

$$J_0(ik_{\mathcal{E}r}) = \sum_{j=0}^{\infty} \frac{\lambda_{\mathcal{E}}^j r^{2j}}{(-4)^j (j!)^2} \quad (23)$$

where  $\lambda_{\mathcal{E}} = (ik_{\mathcal{E}})^2 = -k_{\mathcal{E}}^2$  and  $\gamma$  denotes the Euler-Mascheroni constant.

By letting

$$Y_0(ik_{\mathcal{E}r}) = Y_{01}(ik_{\mathcal{E}r}) + Y_{02}(ik_{\mathcal{E}r}) \quad (24)$$

where

$$Y_{01}(ik_{\mathcal{E}}r) = \frac{2}{\pi} \left[ \sum_{j=0}^{\infty} \frac{\lambda_{\mathcal{E}}^j r^{2j}}{(-4)^j (j!)^2} (\ln r - S_j) \right] \quad (25)$$

and

$$Y_{02}(ik_{\mathcal{E}}r) = \frac{2}{\pi} \left( \gamma + \ln \frac{ik_{\mathcal{E}}}{2} \right) \sum_{j=0}^{\infty} \frac{\lambda_{\mathcal{E}}^j r^{2j}}{(-4)^j (j!)^2} \quad (26)$$

Eq. (6) becomes

$$G_{\mathcal{E}}(P, Q) = -\frac{1}{4} \left( Y_{01}(ik_{\mathcal{E}}r) - iJ_0(ik_{\mathcal{E}}r) + Y_{02}(ik_{\mathcal{E}}r) \right) = G_{\mathcal{E}1}(P, Q) + G_{\mathcal{E}2}(P, Q) \quad (27)$$

where

$$G_{\mathcal{E}1}(P, Q) = -\frac{1}{4} \left( Y_{01}(ik_{\mathcal{E}}r) - iJ_0(ik_{\mathcal{E}}r) \right) = \sum_{j=0}^{\infty} \lambda_{\mathcal{E}}^j \frac{r^{2j} [2(S_j - \ln r) + i\pi]}{4\pi(-4)^j (j!)^2} \quad (28)$$

and

$$G_{\mathcal{E}2}(P, Q) = -\frac{1}{4} Y_{02}(ik_{\mathcal{E}}r) = \left( \gamma + \ln \frac{ik_{\mathcal{E}}}{2} \right) \sum_{j=0}^{\infty} \lambda_{\mathcal{E}}^j \frac{-r^{2j}}{2\pi(-4)^j (j!)^2} \quad (29)$$

By employing Eqs. (24) through (29), Eq. (21) is transformed into

$$\begin{aligned} c(P)\psi^{\mathcal{E}}(P) &= \sum_{j=0}^{\infty} \lambda_{\mathcal{E}}^j \left\{ \int_{\Gamma} \left[ \bar{G}_{\mathcal{E}1j}(P, Q) \psi_{,n}^{\mathcal{E}}(Q) - \bar{G}_{\mathcal{E}1j,n}(P, Q) \psi^{\mathcal{E}}(Q) \right] dQ \right. \\ &\quad \left. + \eta \int_{\Gamma} \left[ \bar{G}_{\mathcal{E}2j}(P, Q) \psi_{,n}^{\mathcal{E}}(Q) - \bar{G}_{\mathcal{E}2j,n}(P, Q) \psi^{\mathcal{E}}(Q) \right] dQ \right\} \quad (30) \end{aligned}$$

where

$$\eta = \gamma + \ln \frac{ik_{\mathcal{E}}}{2} \quad (31)$$

$$\bar{G}_{\mathcal{E}1j}(P, Q) = \bar{G}_{\mathcal{L}j}(P, Q) = \frac{r^{2j} [2(S_j - \ln r) + i\pi]}{4\pi(-4)^j (j!)^2} \quad (32)$$

$$\bar{G}_{\mathcal{E}2j}(P, Q) = \frac{-r^{2j}}{2\pi(-4)^j (j!)^2} \quad (33)$$

$$\bar{G}_{\mathcal{E}1j,n}(P, Q) = \bar{G}_{\mathcal{L}j,n}(P, Q) = \frac{r^{2j-1} [2j(S_j - \ln r) - 1 + ij\pi]}{2\pi(-4)^j (j!)^2} \frac{\partial r}{\partial \mathbf{n}} \quad (34)$$

$$\bar{G}_{\mathcal{E}2j,n}(P, Q) = \frac{-jr^{2j-1}}{\pi(-4)^j (j!)^2} \frac{\partial r}{\partial \mathbf{n}} \quad (35)$$

In contrast to Eqs. (5) and (6), the fundamental solutions described above are shown to be independent of the wavenumbers  $k_{\mathcal{L}}$  and  $k_{\mathcal{E}}$ , and thereby, independent of the energy  $E$ .

By discretizing Eqs. (20) and (30) with  $N$  boundary elements having a total of  $N_n$  nodes, and using the first  $(m+1)$  terms of the series expansion on the right hand side of these equations, the

following equations are respectively obtained for each source point  $P = 1 \dots N_n$ :

$$\sum_{j=0}^m \lambda_{\mathcal{I}}^j \left( \sum_{k=1}^{N_n} \bar{G}_{jPk}^{\mathcal{I}} \psi_{,nk}^{\mathcal{I}} - \sum_{k=1}^{N_n} \bar{H}_{jPk}^{\mathcal{I}} \psi_k^{\mathcal{I}} \right) = 0 \quad (36)$$

$$\sum_{j=0}^m \lambda_{\mathcal{E}}^j \left( \mu \sum_{k=1}^{N_n} \bar{G}_{jPk}^{\mathcal{E}1} \psi_{,nk}^{\mathcal{I}} - \sum_{k=1}^{N_n} \bar{H}_{jPk}^{\mathcal{E}1} \psi_k^{\mathcal{I}} + \eta \left( \mu \sum_{k=1}^{N_n} \bar{G}_{jPk}^{\mathcal{E}2} \psi_{,nk}^{\mathcal{I}} - \sum_{k=1}^{N_n} \bar{H}_{jPk}^{\mathcal{E}2} \psi_k^{\mathcal{I}} \right) \right) = 0 \quad (37)$$

where Eqs. (9) and (10) are used in Eq. (37) to convert  $\psi_{,nk}^{\mathcal{E}}$  and  $\psi_k^{\mathcal{E}}$  into  $\psi_{,nk}^{\mathcal{I}}$  and  $\psi_k^{\mathcal{I}}$ , respectively.

When applied to all  $N_n$  source points, the two equations above form two linear systems, each containing  $N_n$  equations. These systems can be represented in matrix form as follows:

$$\bar{\mathbf{A}}(E) \mathbf{u}_{\mathcal{I}} = \mathbf{0} \quad (38)$$

$$\bar{\mathbf{B}}(E) \mathbf{u}_{\mathcal{I}} = \mathbf{0} \quad (39)$$

where

$$\bar{\mathbf{A}}(E) = \sum_{j=0}^m \lambda_{\mathcal{I}}^j \bar{\mathbf{A}}_j \quad (40)$$

$$\bar{\mathbf{B}}(E) = \sum_{j=0}^m \lambda_{\mathcal{E}}^j \left( \bar{\mathbf{B}}_{1j} + \eta \bar{\mathbf{B}}_{2j} \right) \quad (41)$$

The condition for having non-trivial solutions for  $\mathbf{u}_{\mathcal{I}}$  is

$$\det[\bar{\mathbf{C}}(E)] = 0 \quad (42)$$

where

$$\bar{\mathbf{C}}(E) = \begin{bmatrix} \bar{\mathbf{A}}(E) \\ \bar{\mathbf{B}}(E) \end{bmatrix} \quad (43)$$

As indicated by Eqs. (40) and (41),  $\bar{\mathbf{A}}$  and  $\bar{\mathbf{B}}$  are polynomials whose coefficients  $\bar{\mathbf{A}}_j$  (for  $\bar{\mathbf{A}}$ ) and  $\bar{\mathbf{B}}_{1j}$  and  $\bar{\mathbf{B}}_{2j}$  (for  $\bar{\mathbf{B}}$ ) are independent of  $E$  (the integrals in Eqs. (20) and (30) are not functions of  $E$ ). This means that, for a given problem, these boundary integrals only need to be evaluated  $(m+1)$  times to determine  $3(m+1)$  coefficients  $\bar{\mathbf{A}}_0, \bar{\mathbf{A}}_1, \dots, \bar{\mathbf{A}}_m, \bar{\mathbf{B}}_{10}, \bar{\mathbf{B}}_{11}, \dots, \bar{\mathbf{B}}_{1m},$  and  $\bar{\mathbf{B}}_{20}, \bar{\mathbf{B}}_{21}, \dots, \bar{\mathbf{B}}_{2m}$ . Then, as polynomials (see Eqs. (40) and (41)),  $\bar{\mathbf{A}}$  and  $\bar{\mathbf{B}}$ , thereby  $\bar{\mathbf{C}}$  can be rapidly computed for every value of  $E$  over the range  $0 < E < V_0$ , even with a very small increment  $\Delta E$ . It should be noted that  $m$  is typically much smaller than  $N_E$ . Consequently, the proposed technique enhances the computational efficiency of searching for the local minima of  $|\det[\bar{\mathbf{C}}(E)]|$  compared to the conventional approach using  $|\det[\mathbf{C}(E)]|$  as described in Section 2.3.

### 3. Numerical Examples

The accuracy and efficiency of the proposed approach were evaluated in this study by analyzing four case studies: the first case has an analytical solution, while the last three had previously been explored by other research teams. These cases centered on straight quantum wires characterized by uniform cross-sections. MATLAB scripts were devised to numerically implement the proposed method employing quadratic boundary elements. In the case of the first three examples, a value of  $m = 30$  is adequate for accurate results. The advantage of the proposed technique is represented by its gain, defined as the ratio of the computational times required by the conventional and the proposed methods.

### 3.1. A quantum wire of circular cross-section

Consider the problem of a GaAs quantum wire embedded in an infinite  $\text{Ga}_{0.63}\text{Al}_{0.37}\text{As}$  barrier region, which was previously studied in [12]. This wire features a circular cross-section with a radius of 5 nm. The parameters for this quantum structure are as follows:  $m_{\mathcal{I}}^* = 0.0665m_0$ ,  $m_{\mathcal{E}}^* = 0.0858m_0$ ,  $V_0 = 320$  meV where  $m_0$  denotes the free electron mass.

In this study, we discretized the circular boundary using 24 uniform quadratic boundary elements. To achieve numerical precision to four decimal places, we selected a value of  $\Delta E = 10^{-4}$  meV. For the energy interval of  $1 \leq E \leq 319$  meV, this necessitated repeating the BEA (conventional method) a total of 3,180,001 times, making it a very time-consuming process.

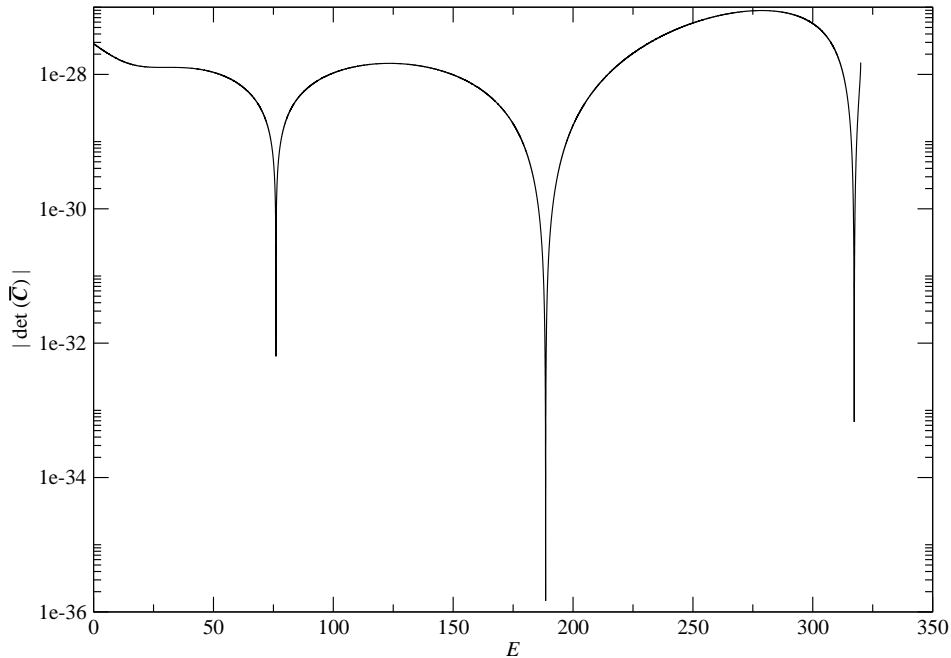


Figure 1: Plot of  $|\det[\bar{\mathcal{C}}(E)]|$  for the quantum wire of circular cross-section.

Analytical Solution [15]	Proposed Method	Conventional Method
76.0663	76.0610 (0.007%)	76.0605 (0.008%)
188.5605	188.5511 (0.005%)	188.5512 (0.005%)
317.2923	317.2861 (0.002%)	317.2878 (0.001%)

Table 1: The energy eigenvalues  $E$  (in meV) for the quantum wire of circular cross-section. The percentage errors are given in parentheses.

Figure 1 illustrates the local minima of  $|\det[\bar{\mathcal{C}}(E)]|$  within the specified interval. All three energy eigenvalues, as determined by the proposed method, demonstrate excellent agreement with both the analytical results [15] and those obtained using the conventional method (see Table 1).



Notably, it is important to highlight that the gain in this case was approximately 1,316.

In the case of a quantum structure exhibiting specific symmetries, such as the quantum wire discussed in this section, the presence of degenerate energy levels may arise. When employing either conventional or proposed methods, it is necessary to conduct further analysis on the wavefunctions corresponding to a given energy eigenvalue. If multiple linearly independent wavefunctions are associated with the same energy eigenvalue, the quantum state at that energy level is considered degenerate. For this problem, the analytical solution [15] indicates that the two quantum states at 188.5605 meV and 317.2923 meV are doubly degenerate.

The next phase in evaluating the proposed technique involves the examination of contour plots depicting the normalized probability density. These plots offer valuable insights into the spatial distribution of electrons at distinct energy levels. Figures 2(a) and 2(b) display contour plots of the normalized probability density for the two highest excited states. In subplot 2(a), at an energy level of 188.551 meV, we observe a distinctive pattern, indicating the preferential localization of electrons within the quantum wire. This pattern changes noticeably in subplot 2(b), corresponding to an energy level of 317.286 meV, reflecting the influence of higher energy states. The contour plots provide a comprehensive view of how the wavefunctions evolve with energy, offering a deeper understanding of the quantum behavior within the wire.

It's important to note that these contour plots can have an infinite number of orientations due to the continuous rotational symmetry inherent in the circular cross-section. Each orientation corresponds to a distinct eigenvector of the nodal normalized wavefunctions. The orientation shown in Figs. 2(a) and 2(b) corresponds to an eigenvector in which the first nodal wavefunction was normalized to a unit value. This particular type of eigenvector also applies to the subsequent contour plots presented in this work.

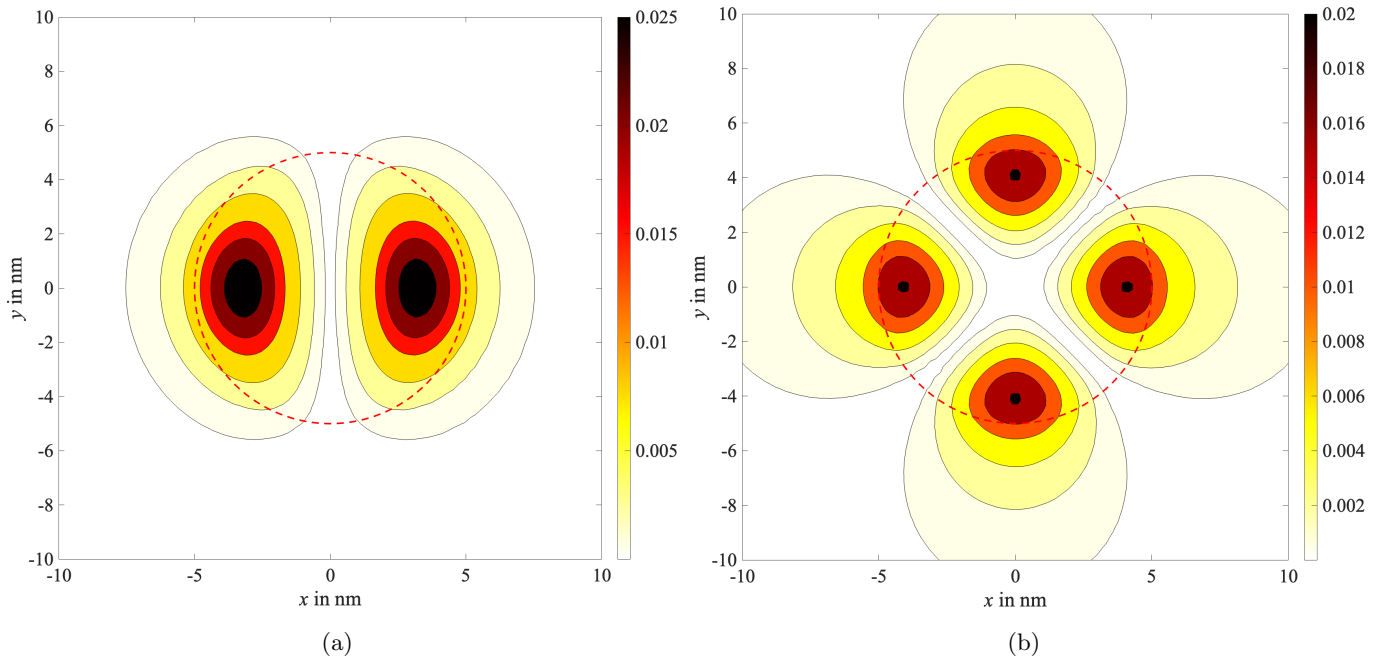


Figure 2: Contour plots of the normalized probability density (in  $\text{nm}^{-2}$ ) for the two highest excited states in a quantum wire of circular cross-section (dashed line) at energy levels of (a)  $E = 188.551$  meV, and (b)  $E = 317.286$  meV.

### 3.2. A quantum wire of square cross-section

This example, as explored in reference [11], features a wire with a square cross-section, each side measuring 10 nm. The effective masses for both the structure and barrier are  $m_{\mathcal{I}}^* = m_{\mathcal{E}}^* = 0.06m_0$ , and the potential barrier is  $V_0 = 300$  meV. A total of 20 uniform quadratic boundary elements was employed in this work to mesh the square boundary, and the numerical results with three decimal digits were achieved using  $\Delta E = 10^{-3}$  meV. By scanning  $|\det[\bar{\mathcal{C}}(E)]|$  within the  $1 \leq E \leq 299$  meV using this step size  $\Delta E$ , three local minima of  $|\det[\bar{\mathcal{C}}(E)]|$  at energy eigenvalues 73.897 meV, 178.190 meV and 274.008 meV were identified as depicted in Fig. 1.

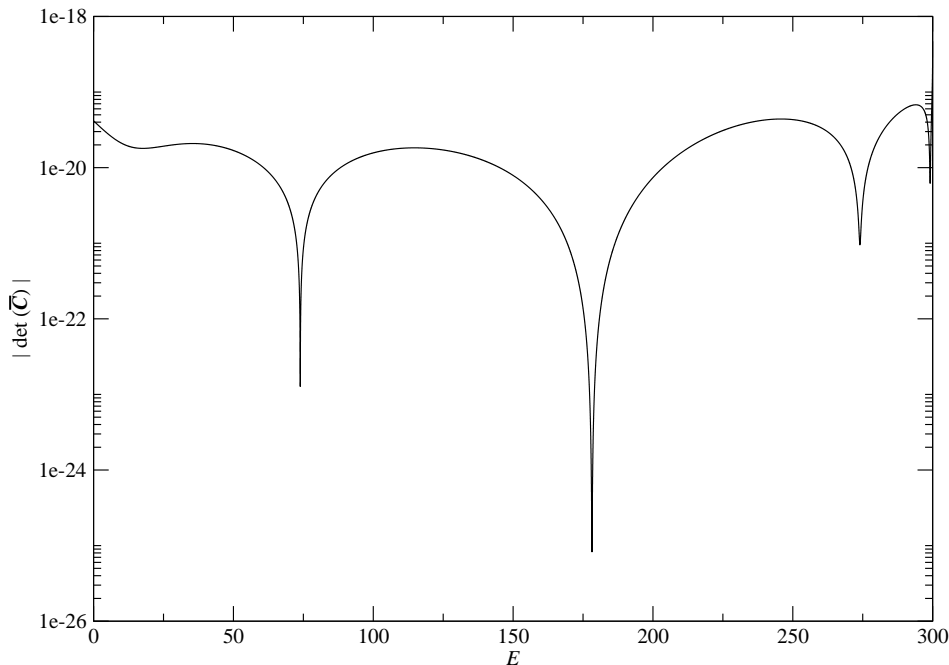


Figure 3: Plot of  $|\det[\bar{\mathcal{C}}(E)]|$  for the quantum wire of square cross-section.

Proposed Method	Conventional Method	Ref. [11]
73.897	73.885 (0.016%)	74.2 (0.410%)
178.190	178.180 (0.006%)	179 (0.455%)
274.008	274.016 (0.003%)	-

Table 2: The energy eigenvalues  $E$  (in meV) for the quantum wire of square cross-section. The percentage discrepancies relative to the proposed method are indicated in parentheses.

As presented in Table 2, the three energy eigenvalues obtained through the proposed method demonstrate a very high level of agreement with those derived from the conventional approach. While the highest energy eigenvalue was not provided in [11], numerical results from the proposed method are consistent with the two lowest energy eigenvalues reported in that reference. Further-

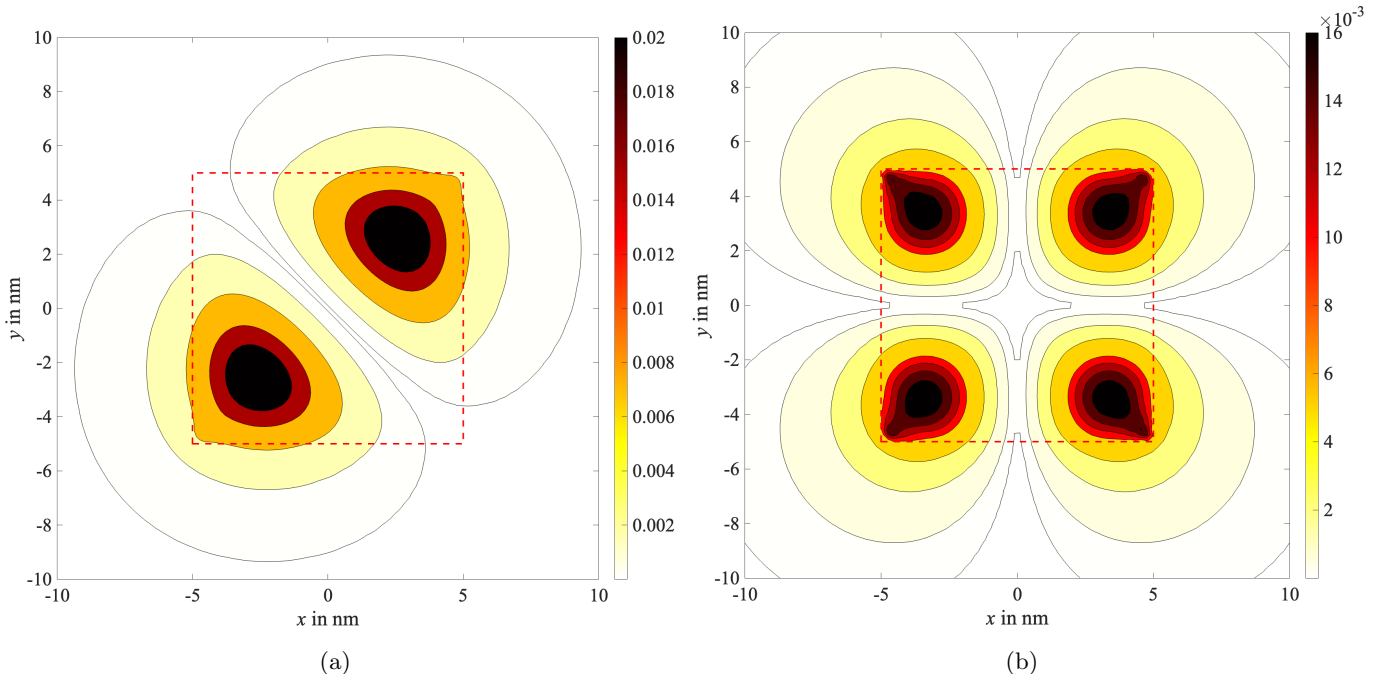


Figure 4: Contour plot of the normalized probability density (in  $\text{nm}^{-2}$ ) for the two highest excited states in a quantum wire with a square cross-section (dashed line) at energy levels of (a)  $E = 178.190$  meV, and (b)  $E = 274.008$  meV.

more, as mentioned in [11], 178.190 meV is a repeated energy eigenvalue. Notably, the proposed method exhibits remarkable computational efficiency, exemplified by the fact that, for this specific problem, the gain was around 1,712.

The contour plots in Figs. 4(a) and 4(b) illustrate the normalized probability density for the two highest excited states at energy levels of 178.190 meV and 274.008 meV within this quantum square wire. The contour plot in subplot 4(a) bears resemblance to the corresponding one found in [11], with the exception of the orientation of the lobes between the two plots. As noted in [11], the excited state at 178.190 meV exhibits double degeneracy. The vertically aligned lobes observed in the same reference were achieved by linearly combining two null vectors, each originating from one of the two degenerate states.

### 3.3. A quantum wire of rectangular cross-section

In this section, the quantum wire case with a rectangular cross-section measuring 20 nm in width and 10 nm in height, as previously examined in [12], was revisited. The material properties remained consistent with those described in Section 3.1, and the barrier potential was maintained at 276 meV. For the BEA in this study, the rectangular interface was discretized using ten uniform elements along the longer side and five uniform elements along the shorter side, resulting in a total of 30 quadratic boundary elements.

Figure 5 depicts ten local minima of  $|\det[\bar{C}(E)]|$  in the interval  $1 \leq E \leq 275$  meV. The results displayed in Table 3 indicate a strong agreement between the numerical outcomes achieved through the proposed method and those documented in [12] and [16]. These results exhibit a percentage discrepancy of less than 0.75%. Moreover, the gain for this particular case was roughly 1,828.

In Fig. 6, a contour plot of the normalized probability density for the highest excited state

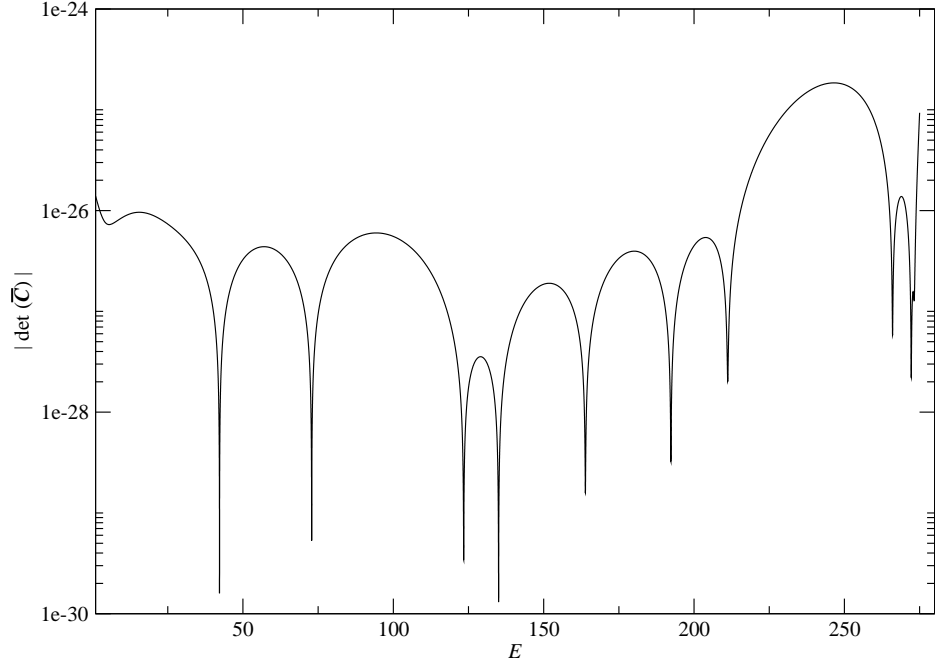


Figure 5: Plot of  $|\det[\bar{\mathbf{C}}(E)]|$  for the quantum wire of rectangular cross-section.

Proposed Method	Ref. [12]	Ref. [16]
42.206	42.276 (0.166%)	42.27 (0.151%)
72.849	73.101 (0.346%)	-
123.397	123.899 (0.407%)	123.86 (0.375%)
135.002	135.177 (0.130%)	135.22 (0.162%)
163.870	164.636 (0.467%)	-
192.297	193.065 (0.399%)	-
211.192	212.717 (0.722%)	-
266.005	266.552 (0.206%)	-
272.225	272.801 (0.212%)	-
273.176	275.049 (0.686%)	-

Table 3: The energy eigenvalues  $E$  (in meV) for the quantum wire of rectangular cross-section. The percentage discrepancies relative to the proposed method are indicated in parentheses.

at an energy eigenvalue of 273.176 meV is depicted, highlighting the presence of point symmetry about the origin (0,0).

### 3.4. A quantum wire of oval cross-section

In this final example, a quantum wire with a stadium-shaped cross-section, a configuration previously examined in [9], was reevaluated. The stadium geometry presents a unique challenge for the

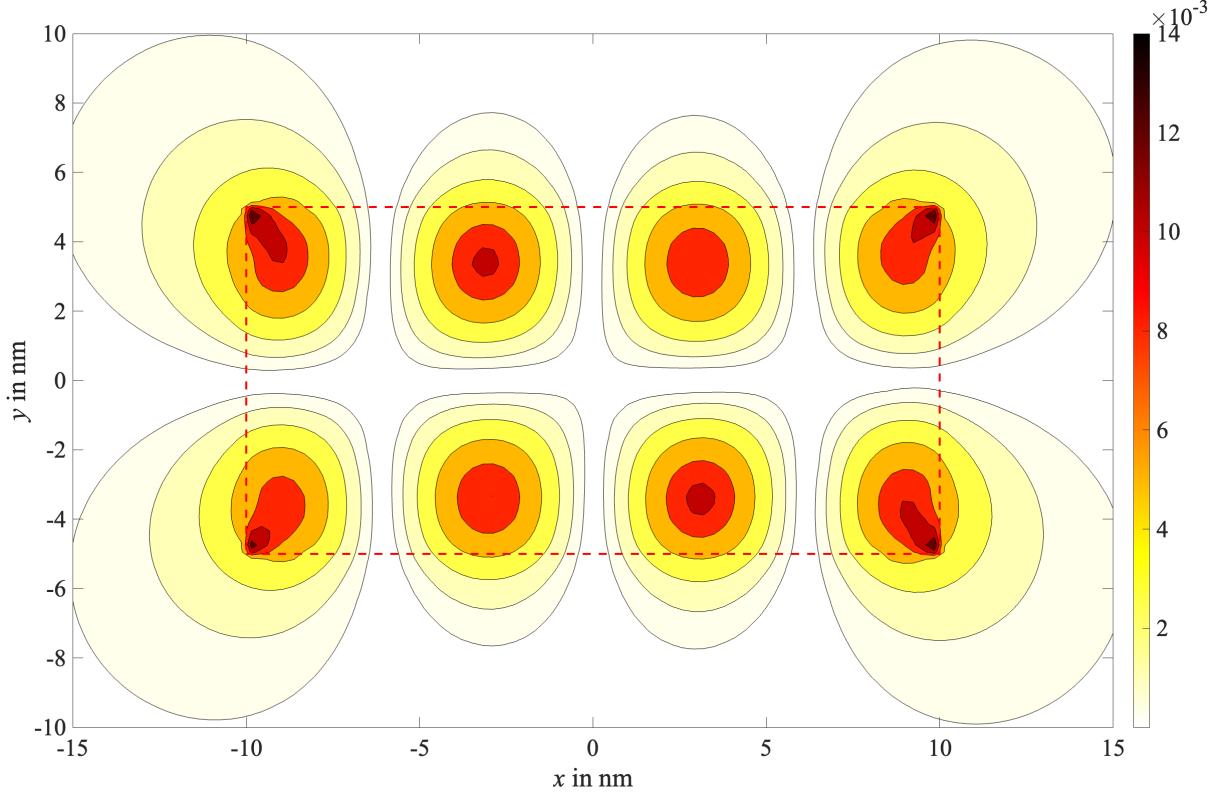


Figure 6: Contour plot of the normalized probability density (in  $\text{nm}^{-2}$ ) for the highest excited state in a quantum wire of rectangular cross-section (dashed line) at energy level of  $E = 273.176$  meV.

analysis of energy eigenvalues, as it combines both curved and flat regions, creating a boundary that demands special consideration. In fact,  $m = 50$  had to be selected to obtain converged numerical results. The structure and barrier both have effective masses of  $0.0665m_0$ , and the potential barrier has a height of 190 meV.

For the given oval boundary, the radius of the semicircles is 12.5 nm, and the length of the line segments is 25 nm. Eight uniform quadratic elements discretize each of the semicircles, while each of the line segments employ four uniform quadratic elements.

A total of 31 energy eigenvalues are visible in Figure 7 as the local minima of  $|\det[\bar{\mathcal{C}}(E)]|$  within the interval  $1 \leq E \leq 189$  meV. For this problem, the conventional method necessitated 985 times more computational time compared to the proposed approach (the gain was approximately 985).

Table 4 reveals an excellent agreement between the numerical results obtained from the proposed and conventional methods, with relative discrepancies mostly below 0.005%. The maximum relative discrepancy, occurring at the energy eigenvalue of 164.705 meV, is 0.011%. It is worth noting that only the highest energy eigenvalue was mentioned in [11], but this value is consistent with the one obtained from the proposed method, with a relative discrepancy of 0.015%.

Figure 8 displays a contour plot depicting the normalized probability density for the highest excited state at the energy eigenvalue of 184.403 meV in the oval quantum wire. It is evident that this contour plot shares similarities with the one featured in [9].

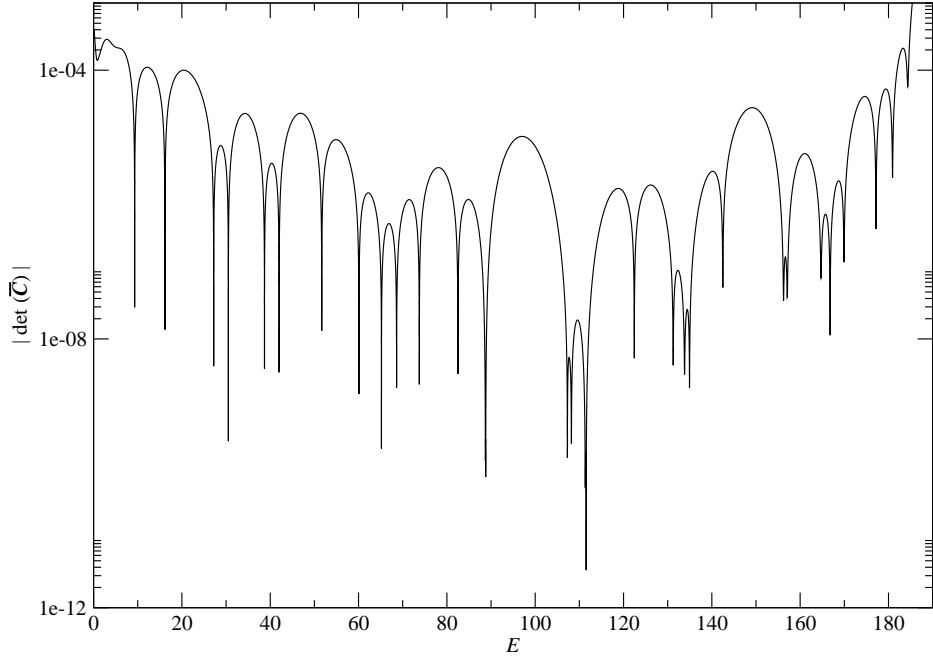


Figure 7: Plot of  $|\det[\bar{\mathbf{C}}(E)]|$  for the quantum wire of oval cross-section.

Proposed Method	Conventional Method	Ref. [9]	Proposed Method	Conventional Method	Ref. [9]
9.296	9.296 (0%)	-	111.539	111.539 (0%)	-
16.156	16.156 (0%)	-	122.442	122.441 (0.001%)	-
27.197	27.197 (0%)	-	131.251	131.249 (0.002%)	-
30.521	30.521 (0%)	-	133.823	133.816 (0.005%)	-
38.700	38.700 (0%)	-	134.946	134.938 (0.006%)	-
42.010	42.010 (0%)	-	142.486	142.475 (0.008%)	-
51.665	51.663 (0.004%)	-	156.239	156.246 (0.004%)	-
60.087	60.085 (0.003%)	-	157.082	157.075 (0.004%)	-
65.188	65.188 (0%)	-	164.722	164.704 (0.011%)	-
68.613	68.609 (0.006%)	-	166.782	166.781 (0.001%)	-
73.760	73.759 (0.001%)	-	169.936	169.935 (0.001%)	-
82.503	82.499 (0.005%)	-	177.169	177.173 (0.002%)	-
88.721	88.721 (0%)	-	180.919	180.917 (0.001%)	-
107.292	107.287 (0.005%)	-	184.373	184.368 (0.003%)	184.4 (0.015%)
108.199	108.194 (0.005%)	-			

Table 4: The energy eigenvalues  $E$  (in meV) for the quantum wire of oval cross-section. The percentage discrepancies relative to the proposed method are given in parentheses.

## 4. Conclusion

This study introduces a highly efficient approach for computing energy eigenvalues in quantum semiconductor heterostructures. The accurate determination of electronic states within these het-

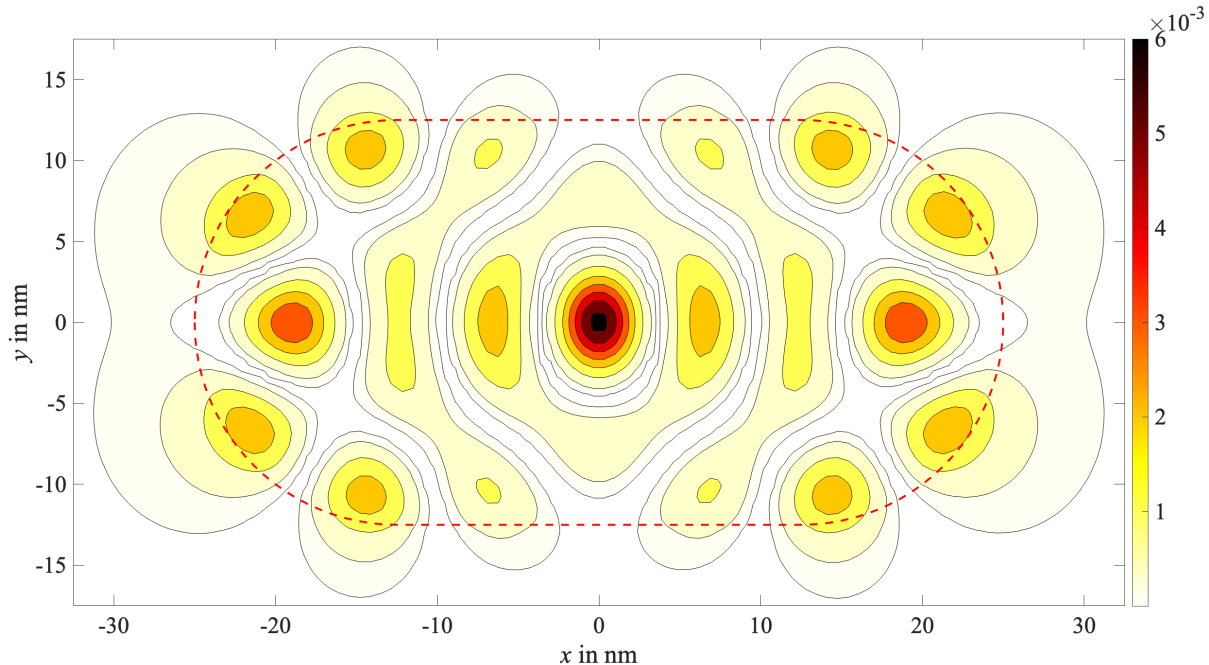


Figure 8: Contour plot of the normalized probability density (in  $\text{nm}^{-2}$ ) for the highest excited state in a stadium quantum wire (dashed line) at energy level of  $E = 184.373$  meV.

erostructures is of paramount importance for a comprehensive understanding of their optical and electronic properties, and as such, it represents a fundamental challenge in the field of semiconductor physics.

The novel approach presented in this work is rooted in the utilization of series expansions of zero-order Bessel functions, which enables the numerical solution of the Schrödinger equation using the boundary integral method for bound electron states in a manner that is not only computationally efficient but also highly accurate.

The credibility and utility of the proposed technique were rigorously tested on problems that have previously been investigated by other research groups. The method's efficacy was demonstrated through the analysis of bound electron states in various quantum wire structures, highlighting its capability to handle complex potential profiles accurately and rapidly. The presented fast boundary integral technique offers a promising tool for the design and optimization of semiconductor devices and paves the way for high-precision simulations of quantum electronic behavior in heterostructures.

In the case of multiply connected domains, Chen *et. al.* [19] have demonstrated that even when utilizing a complex-valued fundamental solution, the BEA of the Helmholtz equation can produce spurious or fictitious eigenvalues. Notably, they found that these spurious eigenvalues are contingent upon the inner boundary of the domain and can be eliminated through the use of the Burton-Miller method [20]. However, to the best of the authors' knowledge, fictitious eigenvalues do not arise in multidomain models employed in the analysis of confined electron states within quantum structures.

## Acknowledgements

J. D. Phan acknowledges the Marilyn Sullivan Scholarship.

## References

- [1] MARTÍN-PALMA, R. J., AND MARTÍNEZ-DUART, J. M., 2017, “Chapter 1 - Low-Dimensional Semiconductors for Nanoelectronics and Nanophotonics,” In *Nanotechnology for Microelectronics and Photonics*, (Second Edition), Elsevier.
- [2] LU, Y., SIGOV, A., RATKIN, L., IVANOV, L. A., AND ZUO, M., 2023, “Quantum computing and industrial information integration: A review,” *Journal of Industrial Information Integration*, **35**, 100511.
- [3] RAM-MOHAN, L. R., SAIGAL, S., DOSSA, D., AND SHERTZER, J., 1990, “The finite element method for the energy eigenvalues of quantum mechanical systems,” *Computers in Physics*, **4**, pp. 50–59.
- [4] CHEN, M., AND POROD, W., AND KIRKNER, D. J., 1994, “Coupled finite element/boundary element method for semiconductor quantum devices with exposed surfaces,” *Journal of Applied Physics*, **75**, pp. 2545–2554.
- [5] RAM-MOHAN, L. R., AND MEYER, J. R., 1995, “Multiband finite element modeling of wavefunction-engineered electro-optical devices,” *Journal of Nonlinear Optical Physics & Materials*, **4**, pp. 191–243.
- [6] HIRAYAMA, K., TANIGUCHI, Y., HAYASHI, Y., AND KOSHIBA, M., 2001, “Finite element analysis of the transmission characteristics of quantum wires in a magnetic field,” *Microelectronics Journal*, **32**, pp. 569–577.
- [7] MOMMADIA, O., HBIBI, M., CHOUF, S., BOUSSETTA, R., CHNAFI, M., EL MOUSSAOUY, A., DUQUE, C. M., AND DUQUE, C. A., 2023, “Behavior of optoelectronic properties of exciton–phonon in a multilayered cylindrical quantum well wires-dot with two finite confinement potentials structures,” *Materials Science in Semiconductor Processing*, **32**, pp. 569–577.
- [8] KNIPP, P. A., AND REINECKE, T. L., 1994, “Boundary element method for calculating electron and photon states in quantum wires and related nanostructures,” *Superlattices and Microstructures*, **16**, pp. 201–204.
- [9] KNIPP, P. A., AND REINECKE, T. L., 1996, “Boundary-element method for the calculation of electronic states in semiconductor nanostructures,” *Physical Review B*, **54**, pp. 1880–1891.
- [10] KOSZTIN, I., AND SCHULTEN, K., 1997, “Boundary integral method for stationary states of two-dimensional quantum systems”, *International Journal of Modern Physics C*, **8**, pp. 293–325.
- [11] GELBARD, F., AND MALLOY, K. J., 2001, “Modeling Quantum Structures with the Boundary Element Method,” *Journal of Computational Physics*, **172**, pp. 19–39.
- [12] GOSPAVIC, R., POPOV, V., AND TODOROVIC, G., 2008, “Boundary element — dual reciprocity formulation for bound electron states in semiconductor quantum wires,” *Computer Physics Communications*, **168**, 107805.



- [13] HOHENESTER, U., 2015, “Quantum corrected model for plasmonic nanoparticles: A boundary element method implementation,” *Physical Review B*, **91**, 205436.
- [14] RAM-MOHAN, L. R., 2002, *Finite Element and Boundary Element Applications to Quantum Mechanics*, Oxford University Press, NY.
- [15] HARRISON, P., AND VALAVANIS, A., 2016, *Quantum Wells, Wires and Dots*, John Wiley & Sons, Inc., West Sussex, UK.
- [16] POKATILOV, E. P., FONOBEROV, V. A., BALABAN, S. N., AND FOMIN, V. M., 2000, “Electron states in rectangular quantum well wires (single wires, finite and infinite lattices),” *Journal of Physics: Condensed Matter*, **12**, pp. 9035–9052.
- [17] PHAN, A.-V., AND KARIMAGHAEI, M., 2021, “A standard energy eigenvalue problem for directly solving the stationary states of quantum billiards via boundary integral analysis”, *Forces in Mechanics*, **4**:100027.
- [18] KARIMAGHAEI, M., AND PHAN, A.-V., 2021, “Boundary integral formulation of the standard eigenvalue problem for the 2-D Helmholtz equation”, *Engineering Analysis with Boundary Elements*, **132**, pp. 281-288.
- [19] CHEN, J. T., LIN, J. H., KUO, S. R., AND CHYUAN, S. W., 2001, “Boundary element analysis for the Helmholtz eigenvalue problems with a multiply connected domain,” *Proc. R. Soc. Lond. A*, **457**, pp. 2521–2546.
- [20] BURTON, A. J., AND MILLER, G. F., 1971, “The application of integral equation methods to the numerical solution of some exterior boundary-value problems,” *Proc. R. Soc. Lond. A*, **323**, pp 201–210. “Boundary element analysis for the Helmholtz eigenvalue problems with a multiply connected domain,” *Proc. R. Soc. Lond. A*, **457**, pp. 2521–2546.